

2026-03-11

The self-archived postprint version of this journal article is available at Linköping University Institutional Repository (DiVA):

<https://urn.kb.se/resolve?urn=urn:nbn:se:liu:diva-202531>

A new strategy for boron cluster-based metal boride (Co₂B) synthesis and its applicability to electrocatalytic nitrate reduction

Xuefan Deng, Shiyong Xia, Haixu Zhao, Jiajia Wang, Zhengxi Wang, Artem Kuklin, Hans Agren, Glib Baryshnikov and Haibo Zhang

Chemical Engineering Journal, (2024), 485

Publisher: Elsevier

<https://doi.org/10.1016/j.cej.2024.149639>

N.B.: When citing this work, cite the original publication.

Copyright holder: See original publication



A new strategy for boron cluster-based metal boride (Co₂B) synthesis and its applicability to electrocatalytic nitrate reduction

Xuefan Deng^{[a][b]}, Shiyong Xia^[b], Haixu Zhao^[b], Jiajia Wang^[b], Zhengxi Wang^{*[a]}, Artem Kuklin^[c], Hans Ågren^[c], Glib Baryshnikov^{*[d]} and Haibo Zhang^{*[b]}

[a] School of Nuclear Technology and Chemistry & Biology, Hubei Key Laboratory of Radiation Chemistry and Functional Materials, Hubei University of Science and Technology, Xianning 437100, P. R. China.

[b] College of Chemistry and Molecular Sciences, Engineering Research Center of Organosilicon Compounds & Materials, Ministry of Education and National Demonstration Center for Experimental Chemistry, Wuhan University, Wuhan 430072, PR China.

[c] Division of X-ray Photon Science, Department of Physics and Astronomy, Uppsala University, Box 516, SE-751 20Uppsala, Sweden.

[d] Laboratory of Organic Electronics, Department of Science and Technology, Linköping University, 60174, Norrköping, Sweden.

* Corresponding author E-mail address:

Zhengxi Wang E-mail: Wangzhengxi@hbust.edu.cn

Glib Baryshnikov E-mail: glib.baryshnikov@liu.se

Haibo Zhang E-mail: haibo Zhang1980@gmail.com

Abstract

To achieve efficient conversion of nitrate to ammonia, it is necessary to design and develop electrode materials with high activity and efficiency for the electrocatalytic reduction reaction of nitrate (NO₃RR). Due to its unique semi-metallic properties, the vacancy orbitals of boron are prone to accommodate electrons, so doping element B with transition metals is expected to change the local electronic configuration of the metal, which in turn affects the corresponding catalytic reaction. Here, we propose a new strategy for the preparation of metal borides by using dodecahydro-closo-dodecaborate and Co²⁺ complexed and calcined to prepare a novel metal boride-Co₂B for electrocatalytic nitrate reduction. This modification considerably enhances the performance of NO₃RR. Co₂B exhibited a Faradaic efficiency of NH₄⁺ (FE_{NH4+}) as high as 96.61% at -0.5 V vs. RHE, achieving a remarkable NH₄⁺ yield of 5.73 mg h⁻¹ mg_{cat}⁻¹. This study provides a new approach for designing catalysts for environmentally-friendly ammonia synthesis.

Keywords: nitrate reduction; ammonia; dodecahydro-closo-dodecaborate; metal boride

1. Introduction

The increase in nitrate (NO₃⁻) pollution in aquatic ecosystems and drinking water threatens global nitrogen cycling, with potential implications for human health and the environment[1]. In recent decades, various physical, biological, and chemical methods have been developed to balance the balancing of the global nitrogen cycle[2]. Electrocatalytic nitrate reduction (NO₃RR) is an effective method for nitrate conversion and different compared to other conventional approaches because it uses renewable energy resources without generating secondary waste[3]. Moreover, NO₃RR can be further integrated with renewable energy sources such as solar and wind energy, enhancing system sustainability. As opposed to thermal catalytic reduction of nitrate, NO₃RR does not require the provision of H₂ or other reducing agents. Instead, it uses electricity to reduce protons present in the aqueous phase, thereby converting nitrate into products such as N₂, NH₃, NO, N₂O, and NH₂OH [4-9]. Electrochemical NO₃RR in aqueous solutions involves a proton-coupled electron transfer reaction, with the involvement of either a five-electron reduction leading to the formation of nitrogen gas or an eight-electron complete reduction resulting in the production of ammonia[10]. The significance of the complexity of nitrate reduction is manifested by comparing it with the four-electron oxygen evolution reaction (OER), oxygen reduction reaction (ORR), two-electron hydrogen evolution reaction (HER), or the hydrogen oxidation reaction underscores its significance. The electrochemical reduction of NO₃⁻ to NO₂⁻ is considered as the rate-determining step that controls the overall kinetics of the NO₃⁻ reduction process[11]. Additionally, the NO₃RR rate is directly proportional to the specific surface area, adsorption capacity, and NO₃⁻ concentration of the electrocatalyst[12].

The conversion of NH₄⁺ is regarded as the preferred final product and a thermodynamically stable form of nitrogen. The electrocatalytic reduction mechanism of NO₃⁻ is highly complex because it involves multiple intermediate species (such as NO₂⁻, N₂H₄, H₂NOH, and NO) as the oxidation state of nitrogen transitions from +5 to -3[13]. These intermediate species play crucial roles in explaining the mechanism of the NO₃RR. The

optimal pathway and final products of the electrocatalytic NO_3^- reduction can be modulated by manipulating various factors such as electrode materials, crystal facets, and operating parameters. Therefore, the electrochemical reduction of nitrate to ammonia depends critically on the electrode materials used. Appropriate electrode materials can reduce overpotential, accelerate the reaction rate, and enhance the selectivity toward the reduction product, i.e., ammonia[14]. In recent years, numerous exceptional research studies have explored suitable non-metallic[15, 16], noble metal[17-19], and non-noble metal electrode materials[20-23].

Transition metals, such as copper, iron, nickel, and vanadium are more affordable options and contain numerous electrons in their d-level orbitals, making them highly conducive to redox reactions[24-27]. Moreover, the unfilled d-level orbitals offer greater versatility in coordination and allow for smaller, more flexible bonding angles with a wider range of coordinating agents[28-30]. Moreover, the extensive corrosion of nonprecious-metal electrodes caused by the buildup of OH^- during frequent electrolytic reduction reactions degrades their catalytic performance. Furthermore, Skulason et al. suggest that for the flat (111) or step (211) surfaces on pure transition metals, including those near the top of the activity volcano, have high theoretical overpotentials and are subject to competition from hydrogen evolution reactions[31]. Thus, catalyst materials containing alternative key elements must be explored. In the realm of electroreduction to NH_3 , metal borides have emerged as a novel choice owing to the distinctive electronic orbital arrangement of boron[32-35]. With its semimetallic characterization, boron possesses vacant orbitals that can easily accommodate electrons from transition metals, thereby altering the localized electronic configuration of the metal and consequently influencing the electrocatalytic reaction[36-39].

Presently, the majority of B used to produce metal borides is sourced from a mildly alkaline aqueous solution of BH_4^- (hydrogen and OH^- are released during BH_4^- decomposition), thereby forming metal oxides and hydroxides alongside the metal boride[33, 34]. Our group has explored our efforts to investigating composites that utilize *closo*-dodecahydrododecaborane (*closo*- $[\text{B}_{12}\text{H}_{12}]^{2-}$) as a foundation for various catalytic processes[40], including photo-[41, 42], electro-[43, 44], and thermocatalysis[45, 46].

Under the above premises, boron clusters can be considered as a series source of B owing to their exceptional stability, a composition comprising only two elements B and H, and cation tunability. To investigate the metal borides formed by calcination of boron cluster (*closo*- $[\text{B}_{12}\text{H}_{12}]^{2-}$) with metal precursor and their application in the process of NO_3RR , Co-p composites are prepared by introducing Co^{2+} into N-tetrabutylamine - $[\text{B}_{12}\text{H}_{12}]$ ($\text{TBA}_2[\text{B}_{12}\text{H}_{12}]$) through ion exchange, followed by calcination, thereby producing Co_2B . The introduction of element B from *closo*- $[\text{B}_{12}\text{H}_{12}]^{2-}$ has the potential to modulate the electron distribution of Co, thereby enhancing or synergistically promoting the electrocatalytic process. The results show that the synthesized Co_2B exhibited a Faradaic efficiency of NH_4^+ ($\text{FE}_{\text{NH}_4^+}$) as high as 96.61% at -0.5 V vs. RHE, achieving a remarkable NH_4^+ yield of $5.73 \text{ mg h}^{-1} \text{ mg}_{\text{cat}}^{-1}$. Theoretical and experimental findings suggest that the introduction of B increases the catalytic active site, both Co and B surfaces adsorb NO_3^- , and the further reduction to N is energetically spontaneous. The synergistic effect of the two elements (Co, B) improves the catalytic effect, the Co-terminated surface of Co_2B can more effectively catalyze the initial nitrate reduction

step to form nitrite and provide greater ease of desorption of NH_3 compared to the B-terminated surface. This modification considerably enhances the performance of NO_3RR .

2. Experimental

2.1 Materials and Methods.

All the chemicals and solvents were purchased from Shanghai Macklin Biochemical CO., LTD, and used without further purification. Ultrapure water was used for all processes. PXRD spectra were obtained on Bruker D8 Advance. Fourier Transform Infrared Spectra (FT-IR) were obtained on Thermo iS10 (with 32 scans). The XPS spectra of $\text{Co}_2\text{B}/\text{BCN}$ were recorded on ESCALAB250Xi. The material was prepared into a suspended ethanol solution and dropped on a silicon wafer to air dry. Then, Scanning Electron Microscopy (SEM) images were collected on Zeiss SIGMA (signal acquisition mode: Inens SE2; acceleration voltage: 5.00 kV). The material was prepared into a suspended aqueous solution and dropped on a self-supporting carbon film, and the High-Resolution Transmission Electron Microscopy (HR-TEM) image was recorded on JEM-2100 Plus. Co K-edge analysis was performed with Si (111) crystal monochromators at the BL11B beamlines at the Shanghai Synchrotron Radiation Facility (Shanghai, China). Before the analysis at the beamline, samples were pressed into thin sheets 1 cm in diameter and sealed using Kapton tape film. Co K-edge EXAFS spectra were recorded in transmission mode. The XAFS spectra of the standard samples (Co foil, Co_3O_4 , and CoO) were recorded in transmission mode. The spectra were processed and analyzed using the software codes Athena and Artemis[47]. Inductively coupled plasma emission spectrometry (Optima 5300DV) was used to accurately determine the metal content in materials, and we determined that the Co load in $\text{Co}_2\text{B}/\text{BCN}$ was 13.02%. Nuclear magnetic resonance (NMR) spectra were recorded on a Bruker 400-MHz instrument. The chemical shifts (δ) in the ^1H NMR spectra were accounted in an internal standard (0.0 ppm) in D_2O .

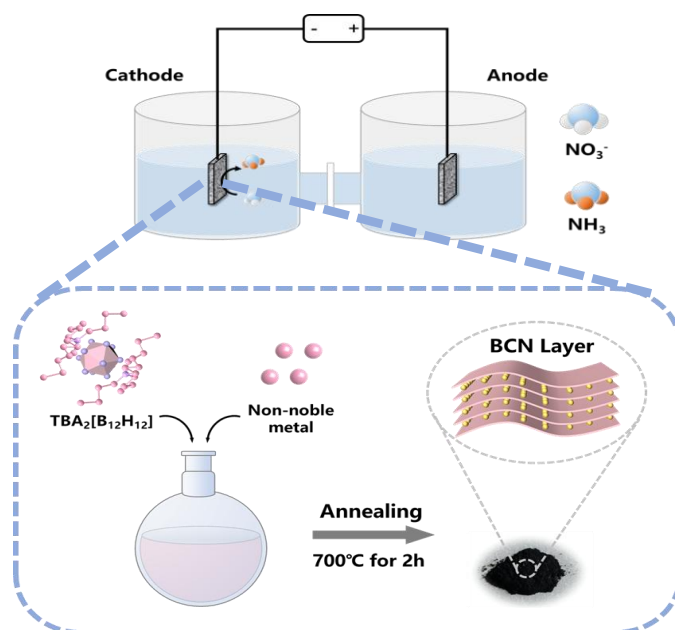
2.2 Preparation of the Catalysts

Preparation of $\text{Cs}_2[\text{B}_{12}\text{H}_{12}]$: $\text{Na}_2[\text{B}_{12}\text{H}_{12}]$ was synthesized using a method in the literature [48].

Preparation of $\text{TBA}_2[\text{B}_{12}\text{H}_{12}]$: 4.074 g (0.01 mol) of $\text{Cs}_2[\text{B}_{12}\text{H}_{12}]$ was dissolved in a 500 mL beaker by adding about 300 mL of deionized water with thorough stirring. Then a slight excess of about 5.0 g of tetrabutylammonium bromide was added to the aqueous solution of boron clusters, and due to the special nature of boron clusters, they will exchange cations to form $\text{TBA}_2[\text{B}_{12}\text{H}_{12}]$. The white solid was filtered and washed with deionized water for three times, and the dried $\text{TBA}_2[\text{B}_{12}\text{H}_{12}]$ was obtained after 12 h at 60 °C.

Preparation of $\text{Co}_2\text{B}/\text{BCN}$: As shown in Scheme 1: 1 mmol of cobalt chloride hexahydrate ($\text{CoCl}_2 \cdot 6\text{H}_2\text{O}$) was dissolved in 30 mL of deionized water, followed by 1 mmol of $\text{TBA}_2[\text{B}_{12}\text{H}_{12}]$ in 10 mL of methanol solution was added dropwise, and the reaction solution was filtered after continued stirring for 30 min and washed with deionized water until the filtrate was colorless, then the micronized color of p- $\text{Co}_2\text{B}/\text{BCN}$ was obtained. The dried p- $\text{Co}_2\text{B}/\text{BCN}$ was put into a porcelain boat and placed in a tube furnace. The black powder $\text{Co}_2\text{B}/\text{BCN}$

was prepared under high purity Ar gas at a starting temperature of 283 K. The temperature was increased at a rate of 10 K min⁻¹ for 69 min to 973 K, and kept for 2 h.



Scheme 1. Preparation pathway for Co₂B/BCN

Scheme 1. Preparation pathway for Co₂B/BCN.

2.3 Electrochemical performance test

Electrochemical testing was conducted at 25°C on an electrochemical workstation (CORRTEST, Wuhan, China) using a double-chamber electrolytic cell (separated by Nafion 117) equipped with a three-electrode system and 75 mL of 0.1-M KOH with 100-mM KNO₃ as the electrolyte. For the catalyst ink, 10.0 mg of CuxCoy-BCN, 0.3 mL of ultrapure water, 0.65 mL of absolute ethyl alcohol, and 50 μL of Nafion (5 wt%) were mixed and then sonicated for >30 min. Subsequently, 20 μL of this catalyst ink was applied to a 1 × 1 m⁻² piece of processed carbon paper to form the working electrode. The reference and counter electrodes were a Hg/HgO electrode and a platinum wire electrode, respectively. Before electrochemical testing, Ar gas was introduced for 30 min to expel air and a cyclic voltammetry curve at 100 mV/s was performed to activate the electrode. Linear sweep voltammetry (LSV) curves and amperometric current–time (*i*–*t*) curves were then determined at different voltages. The formula for RHE conversion is $E_{\text{RHE}} = E_{\text{Hg/HgO}} + 0.059 \text{ pH} + 0.098$.

2.4 Product detection method

The detection of NH₄⁺-N yields: Detection of NH₄⁺-N was performed using indophenol blue colorimetry: six standard solution gradients of 4 mg/L, 2.5 mg/L, 1.6 mg/L, 0.8 mg/L, 0.4 mg/L and 0.1 mg/L of NH₄Cl in 0.1 M KOH solution were prepared. Adding 0.2 mL of 1 wt% sodium nitroprusside solution, 2 mL of 1 M NaOH solution (containing 5 wt% salicylic acid and 5 wt% sodium citrate), and 1 mL of 0.05 M NaClO solution (to be used as needed) to 2 mL gradient standard solutions. After standing for 2 hours, the absorbance at 657

nm was recorded on the ultraviolet spectrophotometer, and the standard curve line was drawn according to the correlation between the absorbance of the ultraviolet spectrophotometer and the concentration of $\text{NH}_4^+\text{-N}$ solution (Figure S1 a). The FE and rate of ammonia production are calculated as follows:

$$r(\text{NH}_4^+) = \frac{C(\text{NH}_4^+) \times V}{t \times m_{\text{cat}}} \quad (1)$$

$$FE(\text{NH}_4^+) = \frac{8 \times 96500 \times m(\text{NH}_4^+)}{17 \times Q} \quad (2)$$

Here, $r(\text{NH}_4^+)$ denotes the rate of ammonia production ($\text{mg h}^{-1} \text{mg}_{\text{cat}}^{-1}$), $c(\text{NH}_4^+)$ represents the concentration of ammonia produced (mg/L), V represents the volume (75 mL), t refers to the time (1 h), $FE(\text{NH}_4^+)$ stands for the Faraday efficiency of ammonia production (%), and Q denotes the quantity of electric charge.

The detection of $\text{NO}_2^-\text{-N}$ yields: Detection of $\text{NO}_2^-\text{-N}$ by colorimetric method. 0.1 g of N-(1-naphthyl)-ethylenediamine hydrochloride, 1.0 g of sulfonamide and 2.94 mL of phosphoric acid were dissolved in 50 mL of deionized water to form Griess color developer. Six standard solutions were prepared in 0.1 M KOH solution at 0.4 mg/L, 0.8 mg/L, 1 mg/L, 1.6 mg/L, 3.2 mg/L, 6.4 mg/L and 6.4 mg/L of NaNO_2 solution. 1 mL of gradients of standard solutions was added to 2 mL of water with 1 mL of Griess colorant. After standing for 1 hour, the absorbance value at 540 nm was recorded on the ultraviolet spectrophotometer, and the standard curve was drawn according to the relationship between absorbance and $\text{NO}_2^-\text{-N}$ solution concentration (Figure S1 b).

$$r(\text{NO}_2^-) = \frac{C(\text{NO}_2^-) \times V}{t \times m_{\text{cat}}} \quad (3)$$

$$FE(\text{NO}_2^-) = \frac{2 \times 96500 \times m(\text{NO}_2^-)}{46 \times Q} \quad (4)$$

Here, $r(\text{NO}_2^-)$ denotes the rate of ammonia production ($\text{mg h}^{-1} \text{mg}_{\text{cat}}^{-1}$), $c(\text{NO}_2^-)$ represents the concentration of ammonia produced (mg/L), V represents the volume (75 mL), t refers to the time (1 h), $FE(\text{NO}_2^-)$ stands for the Faraday efficiency of ammonia production (%), and Q denotes the quantity of electric charge.

2.5 Theoretical Methods

In this study, we employed Density Functional Theory (DFT) within the Vienna Ab-initio Simulation Package (VASP)[49, 50]. The generalized gradient approximation in the form of Perdew-Burke-Ernzerhof functional[51] was utilized with Grimme's D3 correction method[52] to account for van der Waals interactions. The projector augmented wave (PAW)[53] method with a kinetic energy cut-off of 450 eV was used. The first Brillouin zone was sampled by $5 \times 5 \times 1$ k-points utilizing the Monkhorst–Pack scheme[54]. The slab model composed of 6 atomic layers of Co_2B (001) with a vacuum space of at least 15 Å was incorporated to prevent

artificial interactions between neighboring images along the c direction. The energies of HNO_3 , H_2O , and H_2 were computed in a $20 \times 20 \times 20 \text{ \AA}^3$ unit cell with $1 \times 1 \times 1$ k-point sampling.

Convergence criteria were set at $5 \times 10^{-7} \text{ eV/\AA}$ for interatomic forces and 10^{-8} eV for electronic iterations. The atomic structures were visualized using the Visualization for Electronic and Structural Analysis (VESTA) software[55]. PHONOPY code was used to calculate thermodynamic properties[56].

All calculations were carried out within a gas-phase model, considering HNO_3 as a reference that is widely used in literature: $\text{Cu}^0 + \text{HNO}_3 = \text{Cu-NO}_3 + \text{H}^+ + \text{e}^-$, where $\text{H}^+ + \text{e}^- = \frac{1}{2}\text{H}_2$. Subsequent steps involved the reduction of NO_3^- to NH_3 through the stepwise attachment of eight ($\text{H}^+ + \text{e}^-$) species and the elimination of three H_2O molecules in total. Therefore, the final chemical reaction can be expressed as: $\text{HNO}_3 + 8(\text{H}^+ + \text{e}^-) = \text{NH}_3 + 3\text{H}_2\text{O}$,

Gibbs free-energy diagrams were estimated at zero potential ($U = 0$) and a temperature of 300 K using the equation: $\Delta G = \Delta E + \Delta \text{ZPE} - T\Delta S$, where ΔE represents the difference in the total energy of product and reagents, while ΔZPE and ΔS are the differences in zero-point energy and entropy.

3. Results and discussion

3.1 Characterization of $\text{Co}_2\text{B}/\text{BCN}$

To understand the structural characteristics of the as-prepared materials, their microstructure characteristics were further investigated. **Figure 1(a)** and **Figure 1 (b)** displayed the scanning electron microscope (SEM) images of Co-p. The low magnification images show that the material forms an irregular heterojunction structure. This irregularity may be attributed to the material's tendency to agglomerate during the sintering process at elevated temperatures. Moreover, metal nanoparticles appear in the SEM images, suggesting that the prepared nanoparticles are either small in size or encapsulated by the C-layer.

High-resolution transmission electron microscopy (HR-TEM) was used to evaluate the distribution and size of metal nanoparticles more accurately. **Figure 1(c)** shows the HR-TEM images and particle size distribution of Co-p electrode materials. It was observed that the prepared metal nanoparticles were uniformly dispersed with an average particle size of 20.62 nm. **Figure 1(d)** and **Figure 1(e)** show that the lattice spacing of the Co-p nanoparticles is 0.20 nm, which corresponds to the characteristic diffraction peak of Co_2B (200), indicating that most of the Co nanoparticles are Co_2B . Additionally, a layer appears with a lattice stripe spacing of 0.236 nm, corresponding to the (002) crystallographic plane of Co_2B . These results demonstrate that the special metal boride (Co_2B) forms during pyrolysis due to the interaction of boron clusters with Co^{2+} . The high-angle annular dark-field scanning transmission electron microscopy (HAADF-STEM) image (**Figure 1 (f)**) revealed that Co_2B nanoparticles were encapsulated in C- heterojunctions with a relatively dispersed distribution, illustrating that the C- layer serves as a carrier to provide sufficient metal active sites for the catalytic reaction. Energy-dispersive spectroscopy (EDS) demonstrated that element Co is uniformly distributed in the C- layer, which further confirmed the localized distribution of elemental Co, B, C and N in these structures (**Figure 1 (g)-(k)**).

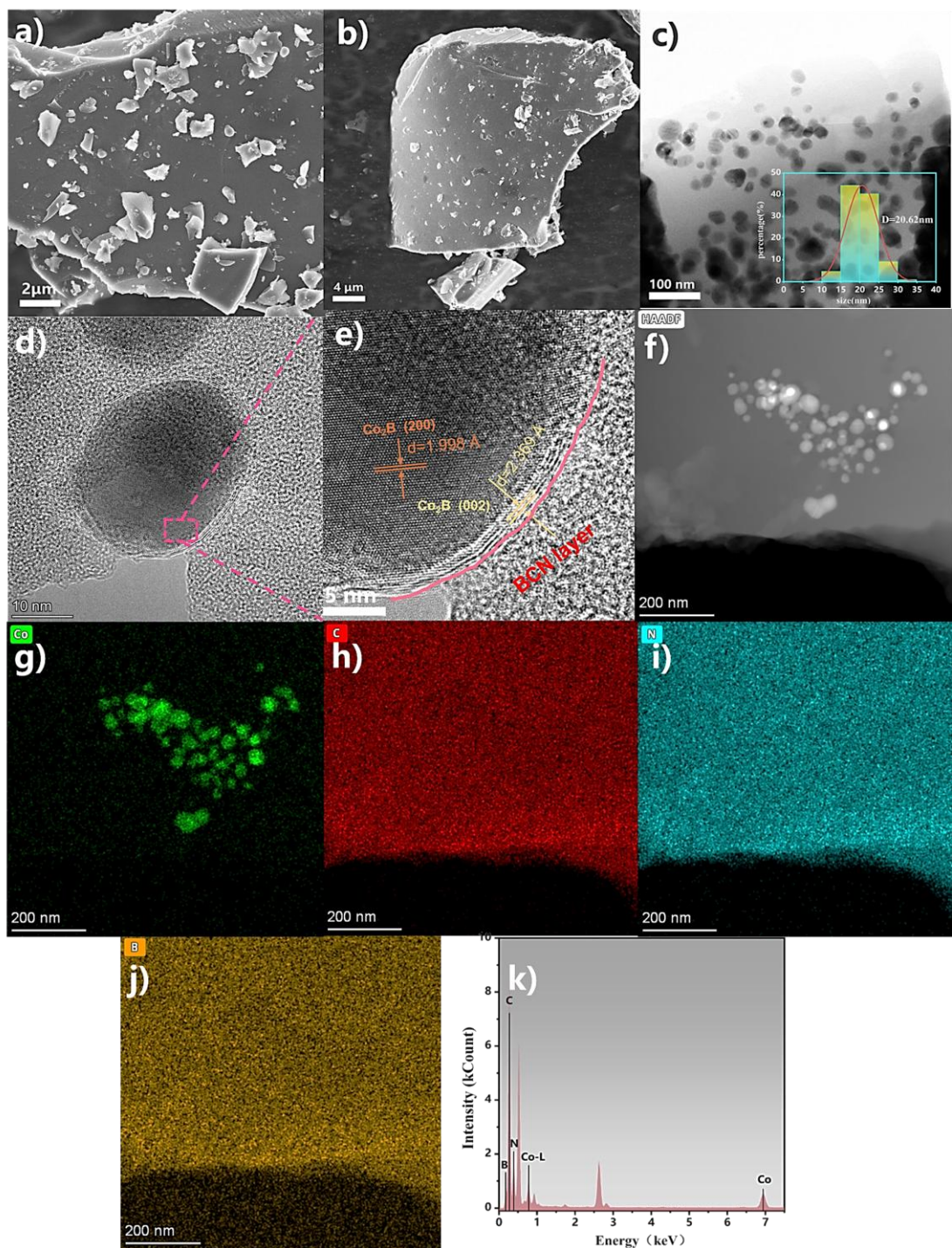


Figure 1. Typical SEM images of Co₂B/BCN (a), (b); HR-TEM images of Co₂B/BCN (c)-(e); HAADF-STEM image of Co₂B/BCN (f); and representative C, N, Co, B elemental mapping of (g), (h), (i), (j) and (k).

Few characterization techniques were applied to further investigate the structural information of the synthesized electrode materials. **Figure 2 (a)** shows the Fourier transform infrared (FT-IR) spectra of the Co-p before and after pyrolysis. The characteristic peaks observed in the precursor p-Co-p are similar to those in the raw material TBA₂[B₁₂H₁₂], with the corresponding telescopic vibrational peaks attributed to the B-H bond of the boron cluster, the in-plane telescopic vibrational peaks of the B-N bond and the telescopic vibrational peaks

of the B-B bond in the B₁₂ backbone[42] appearing near 2500 cm⁻¹, 1370 cm⁻¹ and 1071 cm⁻¹, respectively. In contrast, compared with TBA₂[B₁₂H₁₂], the peaks of p-Co-p near 1378 cm⁻¹ were slightly blueshifted as a result of the broadening of the energy band due to the coordination of metal Co²⁺.

Compared with the TBA₂[B₁₂H₁₂] and the p-Co-p, the characteristic peak of the stretching vibration attributed to the B-H bond near 2500 cm⁻¹ vanishes from the calcined Co-p as well as the characteristic peak of the B-B stretching vibration near 1071 cm⁻¹. This modification generates a new C- substrate after the collapse of the closed cage structure inherent in the B cluster.

Given that no characteristic peaks of metals appear in the FTIR spectra, we used powder X-ray diffraction (PRXD) to further characterize the synthesized electrode materials. **Figure 2 (b)** shows that in addition to the diffraction peaks of TBA₂[B₁₂H₁₂] in the low-angle range $2\theta=10-25^\circ$, p-Co-p exhibits a series of characteristic peaks attributed to the metal in the range of $2\theta=30-50^\circ$, suggesting that TBA₂[B₁₂H₁₂] was coordinated to Co²⁺. After thermal treatment, the diffraction peaks of Co-p in the range of $2\theta=0-20^\circ$ disappear and new metal diffraction peaks emerge, which indicates that the boron clusters have decomposed. The result is consistent with the FTIR results. The diffraction peaks of Co-p at $2\theta = 25.13^\circ, 27.65^\circ, 35.84^\circ, 42.91^\circ, 45.87^\circ, 57.11^\circ, 58.23^\circ,$ and 69.29° correspond to the (110), (101), (200), (002), (211), (202), (310), and (222), respectively. These results are in consistent with those obtained from the Co₂B standard card (PDF#75-1063), indicating that the Co in Co-p is in the form of Co₂B nanoparticles.

X-ray photoelectron spectroscopy (XPS) was used to further characterize the valence and coordination of different elements. The XPS spectra revealed that the 2p_{3/2} and 2p_{1/2} characteristic peaks of Co were located near 779.3 eV and 799.8 eV, respectively (**Figure 2 (c)**), which is consistent with the published results for Co₂B[57]. In addition to the B-N and B-C bonds, the fine spectrum of B 1s of Co-p (**Figure 1 (d)**) show a B-Co bond with a binding energy of 189.3 eV[58], which is blueshifted with respect to the binding energy of pure boron powder (187.2 eV). This phenomenon demonstrates that the local electrons on B transfer to Co, resulting in a weakening of its shielding effect and an increase in binding energy. The local electron transfer could accumulate the electrons on Co and enhances its adsorption capacity to adsorb NO₃⁻, improving the electrocatalytic performance. The characteristic peaks of N 1s in Co-p are located at 397.5 eV, 399.8 eV, and 401.8 eV and are attributed to N-B, respectively, Pyridnic N and Pyrrodic N, respectively (**Figure S2 (a)**), and the fine spectra of C1s show that C-B (282.4 eV), sp²-C (284.7 eV), C-N (286.3 eV), and C-O (287.4 eV), respectively (**Figure S2 (b)**). As shown in **Figure 2 (e)**, the Co K-edge X-ray absorption near-edge spectroscopy (XANES) of Co-p and several reference samples (Co₃O₄, CoO and Co-foil), which reveal that Co in Co/BNC has a valence of +2, which is analogous to the near-edge absorption energy of the reference sample CoO. The Fourier transform extended X-ray absorption fine structure (EXAFS) spectra of Co-p (**Figure 2 (f)**) show Co ligands and peaks at 1.539 and 2.631 Å attributed to the Co-B and Co-B-Co bonds, which were significantly different from the reference samples Co₃O₄, CoO and Co foil. Wavelet transform (WT) analysis of these samples were performed (**Figure 2 (g)-(j)**) to further confirms these results. The intensity near 6.66 Å⁻¹ in Co-p arises from the Co-B bond, whereas that around 11.96 Å⁻¹ arises from the Co-B-Co bond (**Figure 2 (j)**).

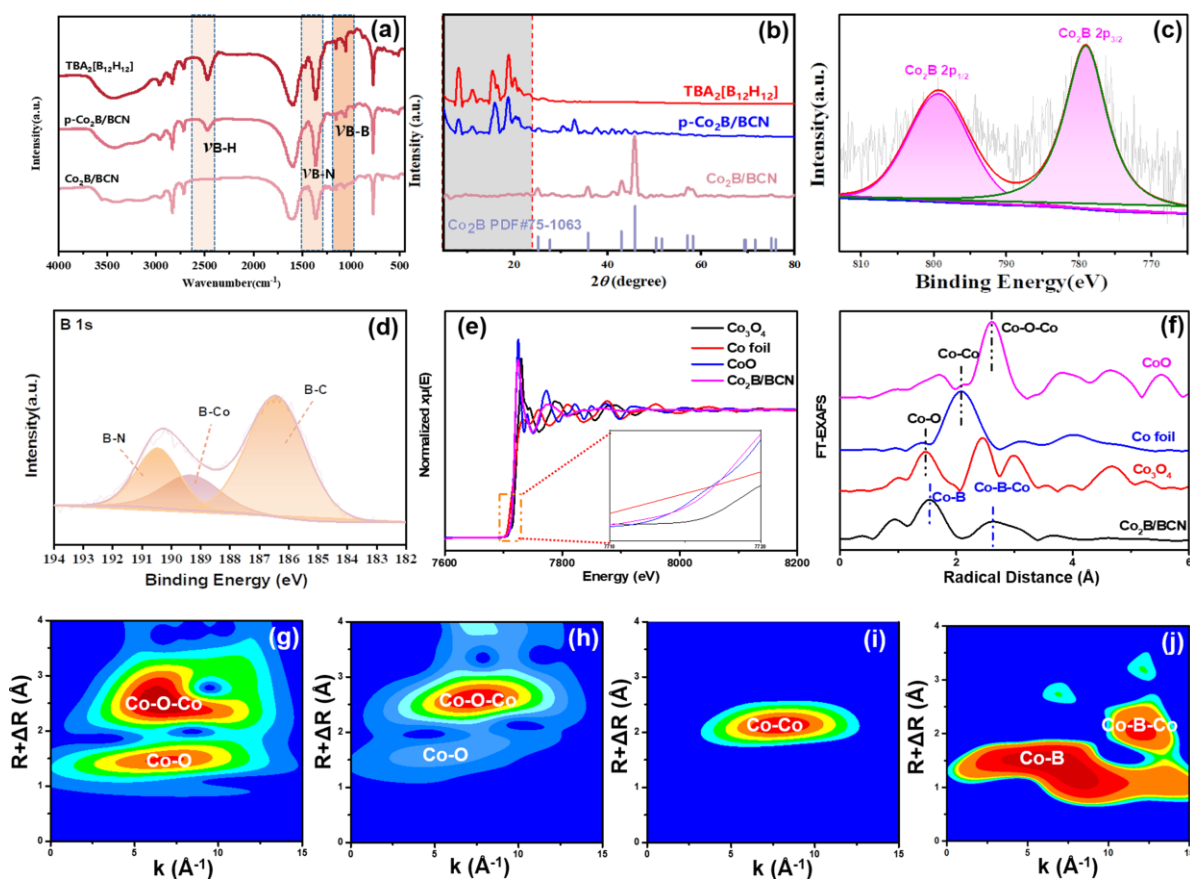


Figure 2. FT-IR spectra of TBA₂[B₁₂H₁₂], p-Co₂B/BCN and Co₂B/BCN (a); PXRD spectra of TBA₂[B₁₂H₁₂], p-Co₂B/BCN and Co₂B/BCN (b); XPS spectra of Co (c); XPS spectra of B (d); Co K-edge XANES spectra (e); EXAFS spectra (f), and WT profiles of Co₃O₄ (g), CoO (h), Co-foil (i) and Co₂B/BCN (j).

3.2 Electrocatalytic reduction of nitrate to ammonium by Co₂B/BCN

The electrochemical performance of Co-p was investigated in detail. As shown in **Figure 3 (a)**, the results indicate that the current densities of the four electrode materials increase greatly compared with those without NO₃⁻ addition, suggesting that these materials are active for the electrochemical reduction of NO₃⁻. Moreover, the current densities are not high prior to adding NO₃⁻, illustrating that the hydrogen evolution reaction (HER) is inactive. Co-p has the largest difference in current density difference, which reaches 45 mA/cm², and the current density increases considerably upon adding NO₃⁻, driving the current density to -75.2 mA/cm² at -1.0 V vs. RHE. Thus, Co-p offers superior electrocatalytic activity for nitrate reduction.

Subsequently, Co-p was applied for constant potential polarization at -0.4 V vs RHE, -0.5 V vs RHE, -0.6 V vs RHE, -0.7 V vs RHE, -0.8 V vs RHE for 1h. The results show that the current density-time (*i-t*) curves at different constant potentials are all independent of time, indicating that the Co-p is stable (**Figure S3**). However, the *i-t* curves reveal a small jagged protrusion as the potential increases above -0.6 V vs. RHE, indicating that the electron transfer rate is too fast at high potentials, which leads to greater OH⁻ and more corrosion of the electrode materials. Furthermore, **Figure 3(b)** shows that the NH₄⁺ yields of Co-p at potentials ranging from -0.4 V vs. RHE to -0.8 V vs. RHE are 4.82 mg h⁻¹ mg_{cat.}⁻¹, 5.73 mg h⁻¹ mg_{cat.}⁻¹, 14.13 mg h⁻¹ mg_{cat.}⁻¹, 15.51 mg h⁻¹

$^1 \text{ mg}_{\text{cat.}}^{-1}$ and $22.54 \text{ mg h}^{-1} \text{ mg}_{\text{cat.}}^{-1}$, respectively. The corresponding NH_4^+ Faraday efficiencies are 83.44%, 96.61%, 90.14%, 93.47%, and 95.32%, respectively, with Co-p recording the highest Faraday efficiency of 96.61% at a potential of -0.5 V vs. RHE, and the ammonia production rate reaches a maximum of $22.54 \text{ mg h}^{-1} \text{ mg}_{\text{cat.}}^{-1}$ at a potential of -0.8 V vs. RHE.

The optimum potential for NH_4^+ selectivity, effective electron utilization, and energy consumption is preferred to be -0.5 vs RHE (**Figure 3 (c)**). During NO_3RR , nitrate is reduced to NH_4^+ through a complex process involving 8 electrons and 10 protons. $\text{NO}_3^- \rightarrow \text{NO}_2^-$ is the main obstacle for effectively removing nitrate from water (i.e., this reaction controls the overall nitrate reduction kinetics). The yield of NO_2^- rises with increasing potential, with Co-p reaching a maximum yield of $7.19 \text{ mg h}^{-1} \text{ mg}_{\text{cat.}}^{-1}$ at -0.7 V vs. RHE, accompanied by the maximum Faraday efficiency of NO_2^- (**Figure S4**). Excessive NO_2^- will occupy the H_{ads} , resulting in the inability to continue the reduction to NH_4^+ .

Thus, the optimal potential is to be -0.5 vs. RHE based on NH_4^+ , effective electron utilization, and energy consumption. Compared to commercial materials, Co-p has a more stable *i-t* curve (**Figure S5**) and the higher yield of NH_4^+ , corresponding to the maximum Faradic efficiency (**Figure S6 (a)**), while the yield of the by-product NO_2^- is relatively low at -0.5 vs RHE (**Figure S6 (b)**). Therefore, the as-prepared Co-p is a good candidate for NO_3RR .

To further investigate the NO_3RR performance, the yields of NH_4^+ and NO_2^- catalyzed by Co-p at different NO_3^- concentrations were explored in detail. The constant potential (-0.5 V vs. RHE) polarization curves of Co-p at NO_3^- concentrations of 20 mg/L, 50 mg/L, 100 mg/L, and 200 mg/L reveal that the current density increases with increasing NO_3^- concentration, while the polarization curves remain constant, illustrating that the exceptional stability and corrosion resistance of Co-p (**Figure S7 (a)**). **Figure 3 (c)** shows the yield of NH_4^+ and the corresponding Faraday efficiency for ppm level NO_3^- concentration (20, 50, 100 and 200mg/L), with a NH_4^+ yield of $8.84 \text{ mg h}^{-1} \text{ mg}_{\text{cat.}}^{-1}$ at a NO_3^- concentration of 200 mg/mL, corresponding to a Faraday efficiency of nearly 100%. Moreover, the nitrite yield and Faraday efficiency are lower in the concentration range of 20-200 mg/mL, which demonstrates the lateral selectivity of NH_4^+ (**Figure S7 (b)**). According to Fick's law, the nitrate concentration determines the diffusion rate of the solution to the cathode surface. A high nitrate concentration increases the number of free catalytic sites on the electrode surface, which determines the reaction rate.

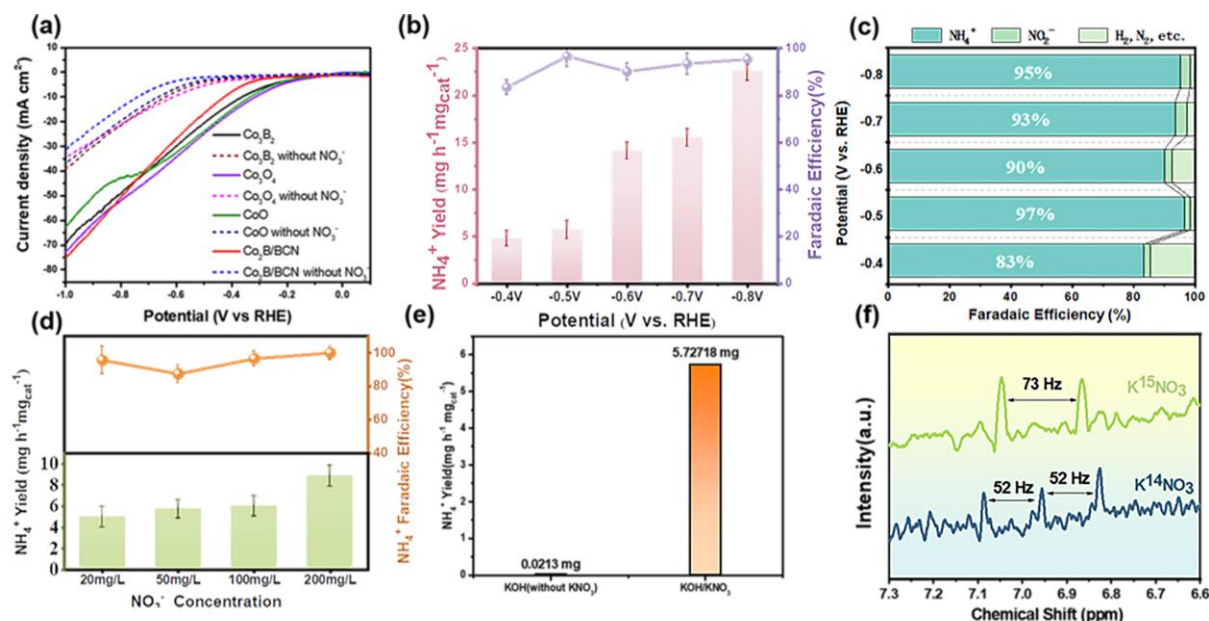


Figure 3. Linear Sweep Voltammetry (LSV) curves of $\text{Co}_2\text{B}/\text{BCN}$, Co_3O_4 , CoO and Co_3B_2 in 0.1M KOH vs. 0.1M $\text{KNO}_3/0.1\text{M KOH}$ (a); yields of NH_4^+ and corresponding faradic efficiencies of $\text{Co}_2\text{B}/\text{BCN}$ at -0.4 V vs RHE, -0.5 V vs RHE, -0.6 V vs RHE, -0.7 V vs RHE, -0.8 V vs RHE, respectively (b); Faradic efficiency of $\text{Co}_2\text{B}/\text{BCN}$ as a percentage of each product at different potentials (c); yield of NH_4^+ and corresponding faradic efficiencies of $\text{Co}_2\text{B}/\text{BCN}$ under different nitrate concentrations at -0.5 V vs. RHE potentials (d); NH_4^+ yield under KOH and KOH/ KNO_3 as electrolyte (e); ^1H NMR spectrum in the electrolyte after constant potential polarization with K^{14}NO_3 and K^{15}NO_3 as N sources (f).

Co-p selectively improves the nitrate surface rather than the symbiotic anions, maximizing the electrode surface area and further enhancing the NO_3RR catalytic effect (**Figure S 7(c)**). **Figures 3 (e) and 3(f)** suggest that the NH_4^+ generated by Co-p in the electrolytic reduction process is all sourced from NO_3^- . When K^{14}NO_3 is used as the N source, three chemical shifts appeared on the ^1H NMR spectrum, with the same peak intensity and spacing (52 Hz), indicating that the peaks are typical of $^{14}\text{NH}_4^+$. In contrast, only two chemical shifts appear on the ^1H NMR spectrum when the N source is K^{15}NO_3 , with consistent peak intensities and spacings of 73 Hz, indicating that these are the characteristic peaks of $^{15}\text{NH}_4^+$. The nitrogen isotope (^{15}N) further demonstrates that all the N in NH_4^+ originates from KNO_3 .

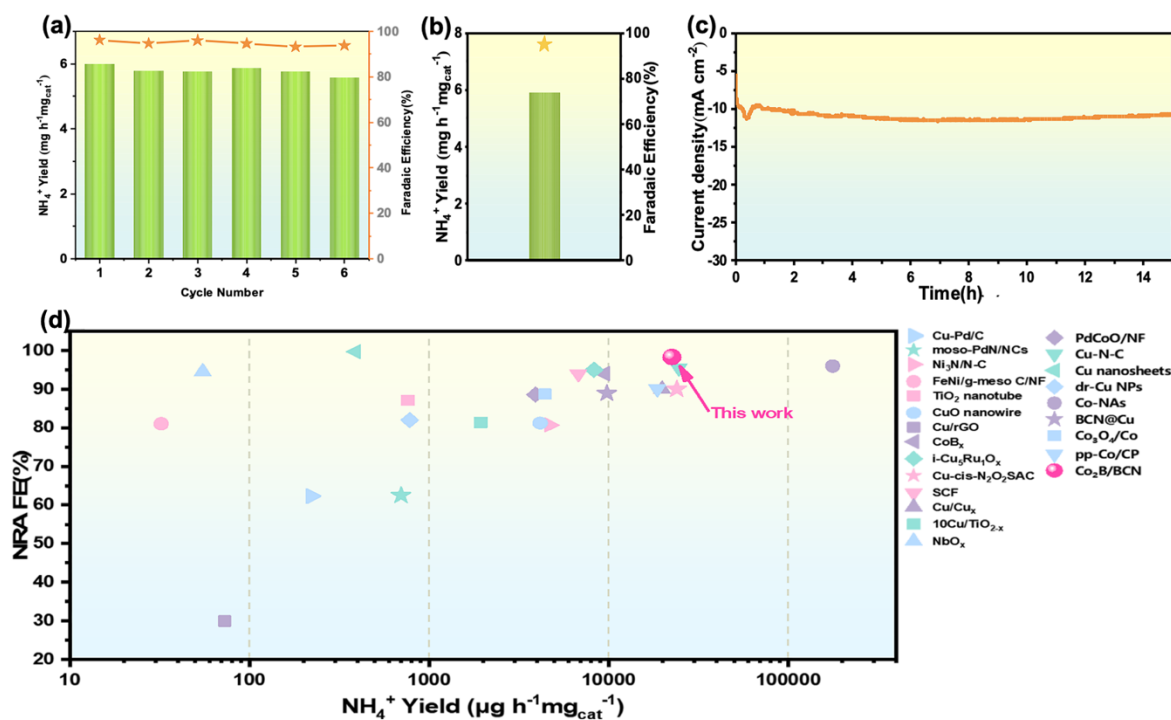


Figure 4. NH₄⁺ yields and Faradic efficiencies of Co₂B/BCN reused 6 times at -0.5 V vs. RHE potentials (a); NH₄⁺ yields and faradic efficiency for Co₂B/BCN electrolyzed continuously for 15h at -0.5 V vs. RHE potential (b), and corresponding to constant potential polarization curves (c); and comparison of NO₃RR performance (d).

Owing to the effective coating of the C-layer, Co-p has better cycling stability. Under the same conditions, the yields of NH₄⁺ catalyzed by Co-p are maintained at ~6.0 mg h⁻¹ mg_{cat}⁻¹ for six cycles, and the Faradic efficiencies all exceed 90%, representing excellent cycle stability (**Figure 4 (a)**). The PXRD spectra of Co-p before and after cycling indicate that the catalyst maintains a relatively well-defined crystalline shape after six cycles, which suggests that the catalyst is relatively stable (**Figure S8**). Moreover, after 15 h of continuous operation at -0.5 V vs. RHE, the current density remains almost constant near -10 mA/cm² and the ammonia-production rate is 5.90 mg h⁻¹ mg_{cat}⁻¹, which is comparable to that of 1 h of electrolysis (**Figure 4 (b)** and **4 (c)**). This illustrates that Co-p can maintain a high activity during NO₃RR for a long time, which provides a theoretical basis for its application in industry. As shown in **Figure 4(d)**, as-prepared Co-p has a moderate-to-high catalytic effect in the current field of efficient NO₃RR reactions[59-77] (the ammonia production rates in the table are normalized). Ammonia production rates in the table are normalized).

3.3 Density Functional Theory

To gain a deeper insight into the catalytic performance of Co₂B nanoparticles integrated into the BCN matrix, we conducted density functional theory (DFT) calculations to assess the free energy diagram. The observed Co₂B nanoparticles demonstrate on-top (002) planes, as determined by TEM. Since there are two possible surfaces: Co-terminated and B-terminated, we studied the conversion of NO₃⁻ to NH₃ on both. Hence, we designed a Co₂B (002) surface composed of six atomic layers. Among several possible positions, we

identified the most stable adsorption configurations and employed them to construct a free energy diagram (see **Figure 5**). For the pristine Co₂B (002) surfaces, our calculations revealed a NO₃⁻ adsorption energy of -1.34 and 1.17 eV for Co- and B-terminated surfaces respectively. Therefore, Co₂B provides a strong fixation of the species.

Our findings indicate that the subsequent reduction of NO₃⁻ to NO₂ and further to N is an energetically favorable process, requiring no additional energy input, along with the subsequent attachment of hydrogen. However, due to the stronger fixation of intermediates on the Co-terminated surface, there is a limiting step of NH₂ formation which can be overcome by the energy generated during the reaction. The desorption energy in for Co-terminated surface is ~0.27 eV lower as compared to the B-terminated one and equals 1.35 eV. The large desorption energy can be explained by the rather strong binding of intermediates on the surface. However, it's worth noting that nitrate in water may involve an increase in energy and would require further estimation. Nevertheless, our simulation results demonstrate that the Co-terminated surface of Co₂B can more effectively catalyze the initial nitrate reduction step to form nitrite and provide greater ease of desorption of NH₃ compared to the B-terminated surface. In summary, the introduction of element B synergizes with element Co to enhance NO₃RR.

Earlier studies have shown that the addition of BCN can enhance NO₃RR by alleviating the limiting step due to charge transfer. However, due to the amorphous nature of BCN in the present study, our theoretical simulations are limited to the explanation effect of Co₂B. We also believe that BCN can significantly improve the efficiency of the nitrate reduction reaction by reducing the size of catalytic centers, which can play a significant role in enhancing NO_x decomposition and increasing a greater number of available active sites. Therefore, small and evenly distributed Co₂B nanoparticles within the BCN matrix provides a substantial active surface area and promotes the catalytic process.

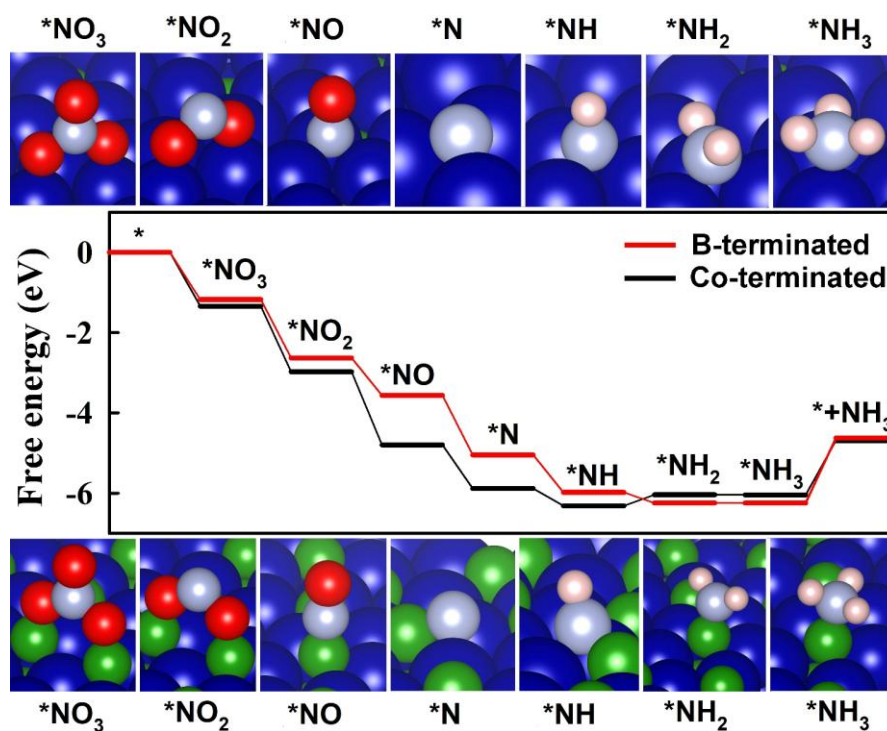


Figure 5. Free-energy diagram of NO_3^- reduction to NH_3 on the Co_2B (002) surface. The optimized geometries of intermediates are shown in the upper and bottom panels for Co- and B-terminated surfaces respectively. Oxygen, cobalt, boron, nitrogen and hydrogen are in red, dark blue, green, light purple and beige respectively.

4. Conclusion

$\text{Co}_2\text{B}/\text{BCN}$ with high crystallinity was prepared by complexing boron clusters ($\text{TBA}_2[\text{B}_{12}\text{H}_{12}]$) with cobalt chloride hexahydrate ($\text{CoCl}_2 \cdot 6\text{H}_2\text{O}$) and calcination. $\text{Co}_2\text{B}/\text{BCN}$ exhibited excellent cyclic and long-time stability, and the ammonia production rate and Faraday efficiency of electrolysis remain constant over 6 cycles and 15 h. This can be attributed to the fact that the $\text{Co}_2\text{B}/\text{BCN}$ is a good candidate for NO_3RR . DFT calculations show that the introduction of B increases the catalytic active site, both Co and B surfaces adsorb NO_3^- , and the further reduction to N is energetically spontaneous. The synergistic effect of the two elements (Co, B) improves the catalytic effect the Co-terminated surface of Co_2B can more effectively catalyze the initial nitrate reduction step to form nitrite and provide greater ease of desorption of NH_3 compared to the B-terminated surface. The introduction of element B synergizes with element Co to enhance NO_3RR .

Acknowledgments

This work was financially supported by the National Natural Science Foundation of China (22179100). This research was also funded by the Foundation of Hubei Provincial Department of Education (Q20222805), Hubei Provincial Department of Science and Technology Project (2023DJC144), the Xianning City Program of Science & Technology (2023ZRKX090), the transverse research and the Scientific Research Foundation of Hubei University of Science and Technology (2023HX026, BK202125, 2022ZX07). A.V.K. acknowledges Olle Engkvist Byggnästare foundation for the support under contract no. 212-0178. The authors also acknowledge the Swedish National Infrastructure for Computing (SNIC 2022-3-34 and NAISS 2023/5-77) at the National Supercomputer Centre of Linköping University (Sweden) partially funded by the Swedish Research Council through grant agreement no. 2018-05973.

References

- [1] N. Gruber, J.N. Galloway, An Earth-system perspective of the global nitrogen cycle, *Nature* 451(7176) (2008) 293-296. <https://doi.org/10.1038/nature06592>.
- [2] B.M. Hoffman, D. Lukoyanov, Z.Y. Yang, D.R. Dean, L.C. Seefeldt, Mechanism of Nitrogen Fixation by Nitrogenase: The Next Stage, *Chemical Reviews* 114(8) (2014) 4041-4062. <https://doi.org/10.1021/cr400641x>.
- [3] S. Wang, H.X. Gao, L. Li, K.S. Hui, D.A. Dinh, S.X. Wu, S. Kumar, F.M. Chen, Z.P. Shao, K.N. Hui, High-throughput identification of highly active and selective single-atom catalysts for electrochemical ammonia synthesis through nitrate reduction, *Nano Energy* 100 (2022). <https://doi.org/10.1016/j.nanoen.2022.107517>.
- [4] W. Ye, M. Arif, X. Fang, M.A. Mushtaq, X. Chen, D. Yan, Efficient Photoelectrochemical Route for the Ambient Reduction of N₂ to NH₃ Based on Nanojunctions Assembled from MoS₂ Nanosheets and TiO₂, *ACS Applied Materials & Interfaces* 11(32) (2019) 28809-28817. <https://doi.org/10.1021/acsami.9b06596>.
- [5] S. Sultana, S. Mansingh, K.M. Parida, Phosphide protected FeS₂ anchored oxygen defect oriented CeO₂NS based ternary hybrid for electrocatalytic and photocatalytic N₂ reduction to NH₃, *Journal of Materials Chemistry A* 7(15) (2019) 9145-9153. <https://doi.org/10.1039/C8TA11437D>.
- [6] S. Mansingh, K.K. Das, S. Sultana, K. Parida, Recent advances in wireless photofixation of dinitrogen to ammonia under the ambient condition: A review, *Journal of Photochemistry and Photobiology C: Photochemistry Reviews* 47 (2021) 100402. <https://doi.org/https://doi.org/10.1016/j.jphotochemrev.2021.100402>.
- [7] S. Mansingh, S. Sultana, R. Acharya, M.K. Ghosh, K.M. Parida, Efficient Photon Conversion via Double Charge Dynamics CeO₂-BiFeO₃ p-n Heterojunction Photocatalyst Promising toward N₂ Fixation and Phenol-Cr(VI) Detoxification, *Inorganic chemistry* 59(6) (2020) 3856-3873. <https://doi.org/10.1021/acs.inorgchem.9b03526>.
- [8] S. Sultana, L. Paramanik, S. Mansingh, K. Parida, Robust Photoelectrochemical Route for the Ambient Fixation of Dinitrogen into Ammonia over a Nanojunction Assembled from Ceria and an Iron Boride/Phosphide Cocatalyst, *Inorganic chemistry* 61(1) (2022) 131-140. <https://doi.org/10.1021/acs.inorgchem.1c02504>.
- [9] S. Mansingh, S. Subudhi, S. Sultana, G. Swain, K. Parida, Cerium-Based Metal-Organic Framework Nanorods Nucleated on CeO₂ Nanosheets for Photocatalytic N₂ Fixation and Water Oxidation, *ACS Applied Nano Materials* 4(9) (2021) 9635-9652. <https://doi.org/10.1021/acsanm.1c02043>.
- [10] G.-F. Chen, Y. Yuan, H. Jiang, S.-Y. Ren, L.-X. Ding, L. Ma, T. Wu, J. Lu, H. Wang, Electrochemical reduction of nitrate to ammonia via direct eight-electron transfer using a copper-molecular solid catalyst, *Nature Energy* 5(8) (2020) 605-613. <https://doi.org/10.1038/s41560-020-0654-1>.
- [11] G.E. Dima, G.L. Beltramo, M.T.M. Koper, Nitrate reduction on single-crystal platinum electrodes, *Electrochimica Acta* 50(21) (2005) 4318-4326. <https://doi.org/https://doi.org/10.1016/j.electacta.2005.02.093>.
- [12] I. Katsounaros, G. Kyriacou, Influence of the concentration and the nature of the supporting electrolyte on the electrochemical reduction of nitrate on tin cathode, *Electrochimica Acta* 52(23) (2007) 6412-6420. <https://doi.org/https://doi.org/10.1016/j.electacta.2007.04.050>.
- [13] S. Garcia-Segura, M. Lanzarini-Lopes, K. Hristovski, P. Westerhoff, Electrocatalytic reduction of nitrate: Fundamentals to full-scale water treatment applications, *Applied Catalysis B: Environmental* 236 (2018) 546-568.

<https://doi.org/https://doi.org/10.1016/j.apcatb.2018.05.041>.

[14] J. Yang, F. Calle-Vallejo, M. Duca, M.T.M. Koper, Electrocatalytic Reduction of Nitrate on a Pt Electrode Modified by p-Block Metal Adatoms in Acid Solution, 5(7) (2013) 1773-1783. <https://doi.org/https://doi.org/10.1002/cctc.201300075>.

[15] J. Ding, W. Li, Q.-L. Zhao, K. Wang, Z. Zheng, Y.-Z. Gao, Electroreduction of nitrate in water: Role of cathode and cell configuration, Chemical Engineering Journal 271 (2015) 252-259. <https://doi.org/https://doi.org/10.1016/j.cej.2015.03.001>.

[16] Y. Huang, J. Long, Y. Wang, N. Meng, Y. Yu, S. Lu, J. Xiao, B. Zhang, Engineering Nitrogen Vacancy in Polymeric Carbon Nitride for Nitrate Electroreduction to Ammonia, ACS Applied Materials & Interfaces 13(46) (2021) 54967-54973. <https://doi.org/10.1021/acscami.1c15206>.

[17] P.B. Kettler, Platinum Group Metals in Catalysis: Fabrication of Catalysts and Catalyst Precursors, Organic Process Research & Development 7(3) (2003) 342-354. <https://doi.org/10.1021/op034017o>.

[18] H.-J. Chun, V. Apaja, A. Clayborne, K. Honkala, J. Greeley, Atomistic Insights into Nitrogen-Cycle Electrochemistry: A Combined DFT and Kinetic Monte Carlo Analysis of NO Electrochemical Reduction on Pt(100), ACS Catalysis 7(6) (2017) 3869-3882. <https://doi.org/10.1021/acscatal.7b00547>.

[19] Y. Arikawa, Y. Otsubo, H. Fujino, S. Horiuchi, E. Sakuda, K. Umakoshi, Nitrite Reduction Cycle on a Dinuclear Ruthenium Complex Producing Ammonia, Journal of the American Chemical Society 140(2) (2018) 842-847. <https://doi.org/10.1021/jacs.7b12020>.

[20] Z.-Y. Wu, M. Karamad, X. Yong, Q. Huang, D.A. Cullen, P. Zhu, C. Xia, Q. Xiao, M. Shakouri, F.-Y. Chen, J.Y. Kim, Y. Xia, K. Heck, Y. Hu, M.S. Wong, Q. Li, I. Gates, S. Siahrostami, H. Wang, Electrochemical ammonia synthesis via nitrate reduction on Fe single atom catalyst, Nature Communications 12(1) (2021) 2870. <https://doi.org/10.1038/s41467-021-23115-x>.

[21] M. Hong, Q. Wang, J. Sun, C. Wu, A highly active copper-nanoparticle-based nitrate reduction electrocatalyst prepared by in situ electrodeposition and annealing, Science of The Total Environment 827 (2022) 154349. <https://doi.org/https://doi.org/10.1016/j.scitotenv.2022.154349>.

[22] W.-D. Zhang, H. Dong, L. Zhou, H. Xu, H.-R. Wang, X. Yan, Y. Jiang, J. Zhang, Z.-G. Gu, Fe single-atom catalysts with pre-organized coordination structure for efficient electrochemical nitrate reduction to ammonia, Appl. Catal. B. Environ. 317 (2022) 121750. <https://doi.org/https://doi.org/10.1016/j.apcatb.2022.121750>.

[23] H. Wang, S. Man, H. Wang, V. Presser, Q. Yan, Y. Zhang, Grave-to-cradle upcycling of harmful algal biomass into atomically dispersed iron catalyst for efficient ammonia electrosynthesis from nitrate, Appl. Catal. B. Environ. 332 (2023) 122778. <https://doi.org/https://doi.org/10.1016/j.apcatb.2023.122778>.

[24] D.N. Mueller, M.L. Machala, H. Bluhm, W.C. Chueh, Redox activity of surface oxygen anions in oxygen-deficient perovskite oxides during electrochemical reactions, Nature Communications 6 (2015). <https://doi.org/10.1038/ncomms7097>.

[25] D.A. Kuznetsov, B. Han, Y. Yu, R.R. Rao, J. Hwang, Y. Roman-Leshkov, Y. Shao-Horn, Tuning Redox Transitions via Inductive Effect in Metal Oxides and Complexes, and Implications in Oxygen Electrocatalysis, Joule

- 2(2) (2018) 225-244. <https://doi.org/10.1016/j.joule.2017.11.014>.
- [26] K. Luo, M.R. Roberts, N. Guerrini, N. Tapia-Ruiz, R. Hao, F. Massel, D.M. Pickup, S. Ramos, Y.S. Liu, J.H. Guo, A.V. Chadwick, L.C. Duda, P.G. Bruce, Anion Redox Chemistry in the Cobalt Free 3d Transition Metal Oxide Intercalation Electrode Li Li_{0.2}Ni_{0.2}Mn_{0.6} O-2, *Journal of the American Chemical Society* 138(35) (2016) 11211-11218. <https://doi.org/10.1021/jacs.6b05111>.
- [27] D.L.J. Broere, R. Plessius, J.I. van der Vlugt, New avenues for ligand-mediated processes - expanding metal reactivity by the use of redox-active catechol, o-aminophenol and o-phenylenediamine ligands, *Chemical Society Reviews* 44(19) (2015) 6886-6915. <https://doi.org/10.1039/c5cs00161g>.
- [28] W. Tao, P. Wang, B. Hu, X. Wang, G. Zhou, Accelerating the reaction kinetics from nitrate to ammonia by anion substitution in NiCo-based catalysts, *Journal of Environmental Chemical Engineering* 11(1) (2023) 109117. <https://doi.org/https://doi.org/10.1016/j.jece.2022.109117>.
- [29] Y. Peng, S. Sanati, A. Morsali, H. Garcia, Metal-Organic Frameworks as Electrocatalysts, *Angewandte Chemie-International Edition* (2023). <https://doi.org/10.1002/anie.202214707>.
- [30] J.K. Tian, Y.Q. Shen, P.Z. Liu, H.X. Zhang, B.S. Xu, Y.H. Song, J.G. Liang, J.J. Guo, Recent advances of amorphous-phase-engineered metal-based catalysts for boosted electrocatalysis, *Journal of Materials Science & Technology* 127 (2022) 1-18. <https://doi.org/10.1016/j.jmst.2022.03.021>.
- [31] E. Skúlason, T. Bligaard, S. Gudmundsdóttir, F. Studt, J. Rossmeisl, F. Abild-Pedersen, T. Vegge, H. Jónsson, J.K. Nørskov, A theoretical evaluation of possible transition metal electro-catalysts for N₂ reduction, *Physical Chemistry Chemical Physics* 14(3) (2012) 1235-1245. <https://doi.org/10.1039/C1CP22271F>.
- [32] L.-H. Zhang, Y. Jia, J. Zhan, G. Liu, G. Liu, F. Li, F. Yu, Dopant-Induced Electronic States Regulation Boosting Electroreduction of Dilute Nitrate to Ammonium, 62(22) (2023) e202303483. <https://doi.org/https://doi.org/10.1002/anie.202303483>.
- [33] G. Zhang, F. Wang, Y. Wan, Y. Guo, K. Chu, Iron Diboride (FeB₂) for the Electroreduction of NO to NH₃, *Inorganic chemistry* 62(22) (2023) 8487-8493. <https://doi.org/10.1021/acs.inorgchem.3c01207>.
- [34] G. Zhang, N. Zhang, Y. Guo, X. Zhao, K. Chu, Vanadium Diboride (VB₂) for NO Electroreduction to NH₃, *Inorganic chemistry* 62(23) (2023) 8772-8777. <https://doi.org/10.1021/acs.inorgchem.3c00451>.
- [35] K. Chen, Y. Tian, Y. Li, Y. Liu, K. Chu, Amorphous NiB₂ for electroreduction of NO to NH₃, *Journal of Materials Chemistry A* 11(14) (2023) 7409-7414. <https://doi.org/10.1039/D3TA00394A>.
- [36] J.M.V. Nsanzimana, L. Gong, R. Dangol, V. Reddu, V. Jose, B.Y. Xia, Q. Yan, J.-M. Lee, X. Wang, Tailoring of Metal Boride Morphology via Anion for Efficient Water Oxidation, 9(28) (2019) 1901503. <https://doi.org/https://doi.org/10.1002/aenm.201901503>.
- [37] H. Park, A. Encinas, J.P. Scheifers, Y. Zhang, B.P.T. Fokwa, Boron-Dependency of Molybdenum Boride Electrocatalysts for the Hydrogen Evolution Reaction, 56(20) (2017) 5575-5578. <https://doi.org/https://doi.org/10.1002/anie.201611756>.
- [38] E. Lee, H. Park, H. Joo, B.P.T. Fokwa, Unexpected Correlation Between Boron Chain Condensation and Hydrogen Evolution Reaction (HER) Activity in Highly Active Vanadium Borides: Enabling Predictions,

- Angewandte Chemie (International ed. in English) 59(29) (2020) 11774-11778.
<https://doi.org/10.1002/anie.202000154>.
- [39] X. Zhu, X. Zhou, Y. Jing, Y. Li, Electrochemical synthesis of urea on MBenes, Nature Communications 12(1) (2021) 4080. <https://doi.org/10.1038/s41467-021-24400-5>.
- [40] X. Zhao, Z.Q. Yang, H. Chen, Z.X. Wang, X.H. Zhou, H.B. Zhang, Progress in three-dimensional aromatic-like closo-dodecaborate, Coordination Chemistry Reviews 444 (2021). <https://doi.org/10.1016/j.ccr.2021.214042>.
- [41] X. Deng, S. Xia, H. Zhao, Z. Wang, B. Qi, X. Zhou, H. Zhang, Shape-controlled preparation of nano gold (Au), Au clusters, and Au single atoms based on layered double hydroxide with closo-dodecaborate and their utilization for selective nitrobenzene reduction, Chemical Engineering Journal 467 (2023) 143540. <https://doi.org/https://doi.org/10.1016/j.ccej.2023.143540>.
- [42] X. Deng, F. Yao, Z. Wang, H. Zhao, B. Qi, Y. Zhou, H. Zhang, X. Zhou, Atom-dispersed Au combined with nano-Au on halloysite nanotubes with closo-dodecaborate promotes synergistic effects for enhanced photocatalysis, Journal of Materials Chemistry A 11(2) (2023) 809-817. <https://doi.org/10.1039/D2TA07827A>.
- [43] X. Zhao, M. Chen, Y. Zhou, H. Zhang, G. Hu, Fluorinated MXenes accelerate the hydrogen evolution activity of in situ induced snowflake-like nano-Pt, Journal of Materials Chemistry A 11(11) (2023) 5830-5840. <https://doi.org/10.1039/D2TA09698F>.
- [44] X. Sun, B. Wu, J. Chen, B. Li, C. Cao, L. Fan, Y. Fu, X. Deng, H. Zhang, Self-assembly synthesis of Ru nanoparticles anchored on B, N co-doping carbon support for hydrogen evolution: Electronic state induced by the strong metal-support interactions, International Journal of Hydrogen Energy 48(26) (2023) 9682-9689. <https://doi.org/https://doi.org/10.1016/j.ijhydene.2022.12.143>.
- [45] Z. Wang, Y. Liu, H. Zhang, X. Zhou, Cubic platinum nanoparticles capped with Cs₂[closo-B₁₂H₁₂] as an effective oxidation catalyst for converting methane to ethanol, Journal of Colloid and Interface Science 566 (2020) 135-142. <https://doi.org/https://doi.org/10.1016/j.jcis.2020.01.047>.
- [46] Z.-Y. Yu, L.-L. Wei, X.-Y. Guo, B.-P. Zhang, Q. He, H.-B. Guo, Microstructural evolution, mechanical properties and degradation mechanism of PS-PVD quasi-columnar thermal barrier coatings exposed to glassy CMAS deposits, Rare Metals (2018). <https://doi.org/https://doi.org/10.1007/s12598-018-1128-5>.
- [47] B. Ravel, M. Newville, ATHENA, ARTEMIS, HEPHAESTUS: data analysis for X-ray absorption spectroscopy using IFEFFIT, Journal of synchrotron radiation 12(Pt 4) (2005) 537-41. <https://doi.org/10.1107/s0909049505012719>.
- [48] W.D. Chen, G.T. Wu, T. He, Z. Li, Z.P. Guo, H.K. Liu, Z.G. Huang, P. Chen, An improved synthesis of unsolvated NaB₃H₈ and its application in preparing Na₂B₁₂H₁₂, Int. J. Hydrog. Energy 41(34) (2016) 15471-15476. <https://doi.org/10.1016/j.ijhydene.2016.02.143>.
- [49] G. Kresse, J. Furthmüller, Efficiency of ab-initio total energy calculations for metals and semiconductors using a plane-wave basis set, Computational Materials Science 6(1) (1996) 15-50. [https://doi.org/https://doi.org/10.1016/0927-0256\(96\)00008-0](https://doi.org/https://doi.org/10.1016/0927-0256(96)00008-0).
- [50] G. Kresse, J. Hafner, Ab initio molecular dynamics for liquid metals, Physical Review B 47(1) (1993) 558-561. <https://doi.org/10.1103/PhysRevB.47.558>.

- [51] J.P. Perdew, K. Burke, M. Ernzerhof, Generalized Gradient Approximation Made Simple, *Physical Review Letters* 77(18) (1996) 3865-3868. <https://doi.org/10.1103/PhysRevLett.77.3865>.
- [52] S. Grimme, J. Antony, S. Ehrlich, H.J.T.J.o.c.p. Krieg, A consistent and accurate ab initio parametrization of density functional dispersion correction (DFT-D) for the 94 elements H-Pu, *Physical Review B* 82(15) (2010) 154104.
- [53] P.E. Blöchl, Projector augmented-wave method, *Physical review. B, Condensed matter* 50(24) (1994) 17953-17979. <https://doi.org/10.1103/physrevb.50.17953>.
- [54] H.J. Monkhorst, J.D. Pack, Special points for Brillouin-zone integrations, *Physical Review B* 13(12) (1976) 5188-5192. <https://doi.org/10.1103/PhysRevB.13.5188>.
- [55] K. Momma, F.J.J.o.A.C. Izumi, VESTA 3 for three-dimensional visualization of crystal, volumetric and morphology data, *Journal of Applied Crystallography* 44 (2011) 1272-1276.
- [56] A. Togo, I. Tanaka, First principles phonon calculations in materials science, *Scripta Materialia* 108 (2015) 1-5. <https://doi.org/https://doi.org/10.1016/j.scriptamat.2015.07.021>.
- [57] N. Patel, R. Fernandes, G. Guella, A. Kale, A. Miotello, B. Patton, C. Zanchetta, Structured and Nanoparticle Assembled Co-B Thin Films Prepared by Pulsed Laser Deposition: A Very Efficient Catalyst for Hydrogen Production, *The Journal of Physical Chemistry C* 112(17) (2008) 6968-6976. <https://doi.org/10.1021/jp7104192>.
- [58] Y. Chen, K.Y. Liew, J.L. Li, Size controlled synthesis of Co nanoparticles by combination of organic solvent and surfactant, *Applied Surface Science* 255(7) (2009) 4039-4044. <https://doi.org/10.1016/j.apsusc.2008.10.077>.
- [59] T. Yin, X. Meng, S.T. Wang, X.Y. Yao, N.W. Liu, L. Shi, Study on the adsorption of low-concentration VOCs on zeolite composites based on chemisorption of metal-oxides under dry and wet conditions, *Sep. Purif. Technol.* 280 (2022) 119634. <https://doi.org/https://doi.org/10.1016/j.seppur.2021.119634>.
- [60] L. Sun, B. Liu, Mesoporous PdN Alloy Nanocubes for Efficient Electrochemical Nitrate Reduction to Ammonia, *ACS Applied Materials* 15(1) (2023) 2207305. <https://doi.org/https://doi.org/10.1002/adma.202207305>.
- [61] X. Chen, T. Zhang, M. Kan, D. Song, J. Jia, Y. Zhao, X. Qian, Binderless and Oxygen Vacancies Rich FeNi/Graphitized Mesoporous Carbon/Ni Foam for Electrocatalytic Reduction of Nitrate, *Environmental Science & Technology* 54(20) (2020) 13344-13353. <https://doi.org/10.1021/acs.est.0c05631>.
- [62] R. Jia, Y. Wang, C. Wang, Y. Ling, Y. Yu, B. Zhang, Boosting Selective Nitrate Electroreduction to Ammonium by Constructing Oxygen Vacancies in TiO₂, *ACS Catalysis* 10(6) (2020) 3533-3540. <https://doi.org/10.1021/acscatal.9b05260>.
- [63] D. Yin, Y. Liu, P. Song, P. Chen, X. Liu, L. Cai, L. Zhang, In situ growth of copper/reduced graphene oxide on graphite surfaces for the electrocatalytic reduction of nitrate, *Electrochimica Acta* 324 (2019) 134846. <https://doi.org/https://doi.org/10.1016/j.electacta.2019.134846>.
- [64] C. Chen, K. Li, C. Li, T. Sun, J. Jia, Combination of Pd-Cu Catalysis and Electrolytic H₂ Evolution for Selective Nitrate Reduction Using Protonated Polypyrrole as a Cathode, *Environmental Science & Technology* 53(23) (2019) 13868-13877. <https://doi.org/10.1021/acs.est.9b04447>.
- [65] Y. Shi, S. Xu, F. Li, Electrocatalytic nitrate reduction to ammonia via amorphous cobalt boride††Electronic supplementary information (ESI) available. See DOI: <https://doi.org/10.1039/d2cc02261c>, *Chem. Commun.* 58(62)

(2022) 8714-8717. <https://doi.org/https://doi.org/10.1039/d2cc02261c>.

[66] J. Cai, S. Qin, M.A. Akram, X. Hou, P. Jin, F. Wang, B. Zhu, X. Li, L. Feng, In situ reconstruction enhanced dual-site catalysis towards nitrate electroreduction to ammonia, *Journal of Materials Chemistry A* 10(23) (2022) 12669-12678. <https://doi.org/10.1039/D2TA01772E>.

[67] X.-F. Cheng, J.-H. He, H.-Q. Ji, H.-Y. Zhang, Q. Cao, W.-J. Sun, C.-L. Yan, J.-M. Lu, Coordination Symmetry Breaking of Single-Atom Catalysts for Robust and Efficient Nitrate Electroreduction to Ammonia, 34(36) (2022) 2205767. <https://doi.org/https://doi.org/10.1002/adma.202205767>.

[68] L. Fang, S. Wang, C. Song, S. Lu, X. Yang, X. Qi, H. Liu, Boosting nitrate electroreduction to ammonia via in situ generated stacking faults in oxide-derived copper, *Chemical Engineering Journal* 446 (2022) 137341. <https://doi.org/10.1016/j.cej.2022.137341>.

[69] W. He, J. Zhang, S. Dieckhöfer, S. Varhade, A.C. Brix, A. Lielpetere, S. Seisel, J.R.C. Junqueira, W. Schuhmann, Splicing the active phases of copper/cobalt-based catalysts achieves high-rate tandem electroreduction of nitrate to ammonia, *Nature Communications* 13(1) (2022) 1129. <https://doi.org/10.1038/s41467-022-28728-4>.

[70] X. Zhang, C. Wang, Y. Guo, B. Zhang, Y. Wang, Y. Yu, Cu clusters/TiO_{2-x} with abundant oxygen vacancies for enhanced electrocatalytic nitrate reduction to ammonia, *Journal of Materials Chemistry A* 10(12) (2022) 6448-6453. <https://doi.org/10.1039/D2TA00661H>.

[71] X. Wan, W. Guo, X. Dong, H. Wu, X. Sun, M. Chu, S. Han, J. Zhai, W. Xia, S. Jia, M. He, B. Han, Boosting nitrate electroreduction to ammonia on NbO_x via constructing oxygen vacancies, *Green Chemistry* 24(3) (2022) 1090-1095. <https://doi.org/10.1039/D1GC04483D>.

[72] M. Xu, Q. Xie, D. Duan, Y. Zhang, Y. Zhou, H. Zhou, X. Li, Y. Wang, P. Gao, W. Ye, Atomically Dispersed Cu Sites on Dual-Mesoporous N-Doped Carbon for Efficient Ammonia Electrosynthesis from Nitrate, 15(11) (2022) e202200231. <https://doi.org/https://doi.org/10.1002/cssc.202200231>.

[73] X. Fu, X. Zhao, X. Hu, K. He, Y. Yu, T. Li, Q. Tu, X. Qian, Q. Yue, M.R. Wasielewski, Y. Kang, Alternative route for electrochemical ammonia synthesis by reduction of nitrate on copper nanosheets, *Applied Materials Today* 19 (2020) 100620. <https://doi.org/https://doi.org/10.1016/j.apmt.2020.100620>.

[74] Y. Xu, M. Wang, K. Ren, T. Ren, M. Liu, Z. Wang, X. Li, L. Wang, H. Wang, Atomic defects in pothole-rich two-dimensional copper nanoplates triggering enhanced electrocatalytic selective nitrate-to-ammonia transformation, *Journal of Materials Chemistry A* 9(30) (2021) 16411-16417. <https://doi.org/10.1039/D1TA04743D>.

[75] X. Deng, Y. Yang, L. Wang, X.-Z. Fu, J.-L. Luo, Metallic Co Nanoparticle Catalyzes Selective NH₃ Production from Electrochemical Nitrate Reduction at Current Densities Exceeding 2 A cm⁻², 8(7) (2021) 2004523. <https://doi.org/https://doi.org/10.1002/advs.202004523>.

[76] F. Zhao, G. Hai, X. Li, Z. Jiang, H. Wang, Enhanced electrocatalytic nitrate reduction to ammonia on cobalt oxide nanosheets via multiscale defect modulation, *Chemical Engineering Journal* 461 (2023) 141960. <https://doi.org/https://doi.org/10.1016/j.cej.2023.141960>.

[77] Q. Chen, J. Liang, Q. Liu, K. Dong, L. Yue, P. Wei, Y. Luo, Q. Liu, N. Li, B. Tang, A.A. Alshehri, M.S. Hamdy, Z. Jiang, X. Sun, Co nanoparticle-decorated pomelo-peel-derived carbon enabled high-efficiency electrocatalytic

nitrate reduction to ammonia, Chem. Commun. 58(26) (2022) 4259-4262. <https://doi.org/10.1039/D2CC00952H>.